PCCP

PAPER

View Article Online
View Journal | View Issue

Cite this: *Phys. Chem. Chem. Phys.*, 2026, **28**, 8372

Ultraviolet photoeffects on oxygen–hydrogen interstitial clusters in rutile TiO_2

Heonjae Jeong, †[b] Ian I. Suni,[a] Raylin Chen,[a] Grace McKnight,[b] Elif Ertekin,[b] Xiao Su[a] and Edmund G. Seebauer *[a]

Received 19th October 2025,
Accepted 7th March 2026

DOI: 10.1039/d5cp04013b

rsc.li/pccp

Super-bandgap illumination of semiconductors affects the diffusion and reaction rates of interstitial atoms, but photoeffects on clusters of interstitials remain virtually unexplored. In prototypical metal oxides such as TiO_2 and ZnO, oxygen interstitials (O_i) appear to form stable clusters below about 300 °C. Such cluster formation becomes very important when chemically prepared surfaces of binary oxides submerged in liquid water inject O_i into the solid. New kinetically dominated phenomena occur, such as strong isotopic fractionation, that are influenced by interstitial trapping in clusters. Judicious coordination of temperature and illumination allows optimization of competing kinetic effects, but little is known about the composition of O_i-containing clusters or their photoresponse. This study begins to fill that gap by combining simulations of O_i–H_i clusters by density functional theory (DFT) with self-diffusion measurements of ^{18}O in submerged single-crystal rutile TiO_2(110) under ultraviolet (UV) illumination. The simulations show that O_i–$(H_i)_x$ exists in several isomers, each with multiple charge states that can change upon illumination. The diffusion measurements suggest that UV changes the populations of O_i-containing cluster isomers deep in the solid, and that the details of these changes depend upon the application of potential bias. The results indicate that illumination alters the rate constants for formation or dissociation of $(O_i)_y$–$(H_i)_x$ or alters the concentration of the reactant H_i.

1. Introduction

Super-bandgap illumination of semiconductors has long attracted interest for altering equilibria among point defects[1–3] and affecting their rates of diffusion[4,5] and reaction.[6,7] Photogenerated minority carriers change the defects' charge state or recombine at defects to convert electronic to lattice vibrational energy.[8] Lower temperatures accentuate such effects by decreasing the rate of thermal carrier generation. Illumination and temperature can then work together to affect semiconductor properties,[9,10] or induce "thermo-photocatalysis."[11]

In prototypical metal oxides such as TiO_2 and ZnO, recent experimental evidence suggests that oxygen interstitials (O_i) can react to form clusters that are stable below about 300 °C.[12] Such clustering can neutralize unwanted donors, especially adventitious hydrogen[13] that is common in oxides,[14–18] but also restricts movement of O_i and thereby inhibits removal of potentially unwanted O vacancies (V_O).[19] These effects take on increased importance because of the recent discovery that chemically prepared surfaces of binary oxides submerged in liquid water inject O_i efficiently.[13] This injection provides an effectual pathway for O_i to dominate low-temperature point defect populations.[13,20,21] Submersion temperatures below 100 °C facilitate kinetically dominated phenomena like strong isotopic fractionation.[22,23] Under such conditions, judicious coordination of temperature and illumination permits optimization among competing kinetic effects. However, apart from the special case of UO_2,[24,25] little is known about the composition of O_i-containing clusters in metal oxides or their response to photostimulation. In TiO_2 and ZnO, the preponderance of such clustering appears to involve interstitial hydrogen (H_i).[12]

This work begins to fill these gaps by combining simulations of O_i–H_i clusters using density functional theory (DFT) with self-diffusion measurements of ^{18}O in submerged single-crystal rutile TiO_2(110) illuminated by ultraviolet (UV) light. The DFT simulations show that O_i–$(H_i)_x$ dimers and trimers exist in several isomers, and each has multiple charge states that can change upon illumination. The diffusion measurements indicate that UV changes the populations of O_i-containing cluster isomers deep in the solid, and that the details of these changes depend upon the application of potential bias. The results suggest that illumination alters the rate constants for

[a] *Department of Chemical and Biomolecular Engineering, University of Illinois at Urbana-Champaign, Urbana, Illinois 61801, USA. E-mail: eseebaue@illinois.edu*
[b] *Department of Mechanical Science and Engineering, University of Illinois at Urbana-Champaign, Urbana, Illinois 61801, USA*
† Current address: Department of Mechanical Engineering, Sogang University, Seoul 04107, South Korea.

formation or dissociation of $(O_i)_y$–$(H_i)_x$ or changes the concentration of the reactant H_i.

2. Methods

2.1 Experiments

Experimental literature concerning illumination-stimulated behavior of defects has typically employed measurements of electrical conductivity,[26] dopant compensation,[27–29] solar cell lifetime,[9,30] or oxygen incorporation rate.[10,31,32] The present study measures depth profiles of ^{18}O injected by TiO_2(110) exposed to isotopically enriched water. Isotopic fractionation occurs in this system, resulting in profile metrics that respond to O_i trapping effects in distinct ways. Such differences enable disaggregation of photostimulation effects on trapping *vs.* other physical processes such as injection or site hopping.

Protocols employed procedures for specimen preparation and diffusion under illumination described elsewhere.[13,23,33] Single-crystal specimens of TiO_2(110) (5 × 5 × 0.5 mm, MTI Corp.) were submerged in ^{18}O-labeled water (10 atomic % ^{18}O, Sigma-Aldrich) at constant temperatures (T) ranging from 30–80 °C. The diffusion time was 60 min except as noted below. Crystals were de-greased by 10 min of ultrasonic agitation in acetone, isopropanol, ethanol, and methanol, followed by wet etching (1 : 2, 30% NH_4OH : H_2O) for 40 min at room temperature to remove elemental poisons that inhibit O_i injection.

Diffusion under submersion was studied with UV illumination using a protocol identical to that described previously.[33] Light originated from an inspection lamp (Black-Ray™ B-100AP/R, UVP) operating with a central wavelength of 365 nm. At 25 cm, the lamp produced an intensity on the order of 5 mW cm^{-2} at the surface. The intensity was kept low to minimize possible heating by light absorption. Evidence that such heating was indeed negligible has been presented elsewhere.[33]

Application of potential bias in a conventional three-electrode cell configuration aids the measurement of self-diffusion metrics by increasing their magnitudes.[23] Accordingly, some TiO_2 specimens were immersed for 60 min at constant T with a potential bias applied using a Biologic SP200 potentiostat. The electrical connection to the TiO_2 specimens was a Cu wire attached with double-stick carbon tape covered with Kapton. An Ag/AgCl reference electrode and a Pt counter electrode were employed. Before immersion, 10 min of air bubbling through the aqueous solution with simultaneous air flow through the headspace established liquid–gas equilibrium.

The undoped TiO_2 was electrically insulating and no electrolyte was employed, so no faradaic electrochemistry occurred. Measured currents were small (10–100 nA) and did not correlate with any profile metric. Measurements of pH before and after each experiment hovered near 7 and changed 0.25 pH unit or less. Diffusion metrics did not change with the sign or magnitude of the applied potential. Unfortunately, the mechanism by which applied bias increases the injection flux remains unknown at this point. Applying a bias may unintentionally remove a contaminant that poisons injection sites. Other possible hypotheses include that enhanced electric fields or some form of electrostatic electrochemistry[35,36] could play a role. Investigation of these effects will be the subject of future work.

Surface analysis by X-ray photoelectron spectroscopy (XPS) of specimens treated before diffusion by vacuum annealing, NH_4OH etching or degreasing have been published previously.[34] The spectra showed primarily Ti, O, and C. Surface elemental composition and chemical state varied but did not correlate with experimental conditions. Here we supplemented those studies by measuring XPS spectra on select specimens before and after diffusion with applied bias. Spectra were measured with a Kratos Axis ULTRA instrument using a monochromatic Al Kα source (1486.6 eV). Energies were calibrated based on the C_{1s} peak (284.6 eV) of adventitious carbon. Elemental compositions and chemical state were determined using the CasaXPS software library. The results (Fig. S1 and S2 of the SI) for elemental composition and chemical state of Ti, O and C again show variability but no discernable correlation with experimental conditions.

The surface morphology and roughness were measured for some specimens immediately after surface preparation but before submerged diffusion by atomic force microscopy (AFM) with an MFP-3D instrument in tapping mode. A smaller body of such characterization focused on rms roughness has been reported previously,[34] but the current study examines more specimens and reports additional surface parameters such as skew and kertosis. Specimens were dried in flowing N_2 gas to remove droplets removal after removal from the liquid. For accurate comparison between specimens, the Al-coated silicon probes (Ted Pella Inc.) were changed for every measurement. Each measurement generated 512 × 512 data points. Table T1 in the SI shows that etching with NH_4OH yielded a broader range of rms roughness than simple degreasing, with the average being slightly smoother than simple degreasing. Skew and kurtosis varied considerably, although exceptionally high values were distorted by single large protrusions that could have been foreign particulates or dust.

^{18}O depth profiles were measured *ex situ* by secondary ion mass spectrometry (SIMS) using a PHI-TRIFT III instrument. Depth profiling was accomplished with a 3 keV Cs ion beam having a spot diameter near 0.5 mm. Analysis after each cycle of crater deepening employed a beam of Au at 22 keV. ^{18}O concentrations were calibrated to the known natural abundance of ^{18}O (0.2%) within as-received TiO_2 specimens used as standards. ^{18}O concentrations in deep regions of diffused profiles often departed only a few percent from the natural abundance baseline. Thus, special care was taken to calibrate the ion currents corresponding to ^{16}O and ^{18}O – typically measured daily on standard specimens. After diffusion (or initial etching in liquid), specimens were simply removed from the liquid, which did not wet the surface. Occasional residual drops that adhered were blown off with a gentle stream of air or nitrogen. Diffusion profiles were measured several days to weeks after diffusion at 2–5 different locations on the surface of each specimen.

After diffusion in submersion, some specimens were subjected to stages of annealing lasting 50 min at progressively

higher temperatures between 100 and 300 °C in air using procedures akin to those described elsewhere.[12] SIMS was performed after each stage to ascertain whether spreading of the ^{18}O profile had occurred due to release of O_i due to dissociation of interstitial clusters containing this species.

2.2 DFT calculations

Clusters containing O_i and H_i were relaxed using first-principles DFT simulations.[37,38] The projector augmented wave (PAW) method[39,40] as implemented in the Vienna *ab initio* Simulation Package (VASP)[41,42] was utilized, in conjunction with the Perdew–Burke–Ernzerhof (PBE) approximation to the exchange–correlation functional.[43] Calculations employed a plane-wave basis set with a cutoff energy of 520 eV. The ground state lattice parameters of the conventional unit cell for rutile TiO_2 were determined to be a = 4.648 Å and c = 2.969 Å for a 3 × 3 × 4 supercell, consistent with other computational[44–46] values (experimental values[47–50] are a = 4.59 Å and c = 2.96 Å). Defect structures were modeled in 216-atom supercells using the Monkhorst–Pack scheme[51] with a 2 × 2 × 2 k-point mesh. Geometry optimization of defect structures was performed with a convergence criterion of 1×10^{-6} eV for the total energy and 2×10^{-2} eV Å^{-1} for atomic forces. The bandgap computed from PBE was 1.79 eV, consistent with other reported PBE bandgaps[46,52–54] and showing the expected DFT-PBE underestimate compared to the experimental value of 3.03 eV.[55] To obtain more realistic descriptions of charge transition levels lying outside the PBE bandgap, the PBE band edges were shifted *via* alignment to the band edges of the Heyd–Scuseria–Ernzerhof (HSE06) screened hybrid functional approximation, opening the predicted gap to 3.05 eV.[45,56]

The defect formation energy $E_{form}[X_i^q]$ of a point or cluster defect in charge state q was obtained using the supercell approach:[57–59]

$$E_{form}[X_i^q] = E_{tot}[X_i^q] - E_{tot}[\text{bulk}] - \sum_i n_i\mu_i + qE_F + E_{corr} \quad (1)$$

where $E_{tot}[X_i^q]$ denotes the total energy of the defective supercell and $E_{tot}\lceil$ bulk $\rceil$ is the total energy of the pristine bulk supercell. The term n_i is the number of defective atoms of type i, while μ_i denotes their chemical potential. O_i is mobile, which puts O in the lattice in indirect contact with an external reservoir of O (*i.e.*, air). Thus, the O-rich environment characteristic of water with dissolved air was simulated in eqn (1) using $\mu_O = -5.15$ eV given by half of the energy of the O_2 molecule computed under standard conditions (300 K and 1 atm).

The situation is more complex for H. For TiO_2(110), the surface normal is perpendicular to the c-axis. Interstitial hydrogen diffusion in this direction has a substantial barrier of 1.28 eV,[17,60] which renders H_i incapable of diffusing at 70 °C and eliminates contact between the crystal and an external reservoir of H. Thus, the total amount of hydrogen is not expected to equilibrate with the liquid water environment during the experiment but instead remains constant at the initial adventitious value. However, as discussed below, assessment of which clusters are most likely to form considers reaction energies (E_{rxn}) that do not depend upon the choice of reference states for O and H. Consequently, the chemical potential for H in eqn (1) was set to conditions associated with H in air, given by $\mu_H = \frac{1}{2}[E_{tot}(H_2) + \Delta H + (\text{ZPE} - \text{TS})]$. Here, $E_{tot}(H_2)$ denotes the DFT total energy of the H_2 molecule, ΔH is the enthalpic correction to standard conditions, and ZPE–TS accounts for zero-point energy and thermal entropy contributions.

The Fermi level E_F in eqn (1) accounts for the exchange of electrons from the reference electron reservoir. The energy correction term E_{corr} accounts for the finite-size effects resulting from electrostatic interactions between charged defects in adjacent supercells. The method proposed by Lany and Zunger[58] was employed to calculate the finite size effect corrections for potential alignment $\Delta E_{pa}(D, q)$ and image charge ΔE_i.

The experiments were carried out under kinetically controlled conditions far from equilibrium where it becomes more useful to examine reaction energies instead of formation energies. E_{rxn} compares the formation energy of a cluster $(O_i)_y$–$(H_i)_x$ with the summation of formation energies of its isolated point-defect constituents, as given by:

$$E_{rxn} = E_{form}[(O_i)_y\text{–}(H_i)_x] - y{\cdot}E_{form}[O_i] - x{\cdot}E_{form}[H_i]. \quad (2)$$

Here, $E_{form}[(O_i)_y\text{–}(H_i)_x]$ denotes the formation energy of a cluster comprising y interstitial O atoms and x H atoms, and $E_{form}[O_i]$ and $E_{form}[H_i]$ respectively represent the formation energies of isolated O_i and H_i. A negative value of E_{rxn} signifies exothermicity at 0 K. The calculation does not account for entropy and therefore offers only an approximate guide to the free energy change at the nonzero temperature of the experiment.

3. Results

Fig. 1 illustrates a typical ^{18}O SIMS profile following diffusion. The general shape of this profile matches those reported previously.[22,23] The most dramatic feature is the isotopic fractionation represented by the near-surface "valley" where the ^{18}O concentration drops well below the natural abundance ($C_{nat} = 1.29 \times 10^{20}$ cm^{-3}) of ^{18}O in TiO_2. Isotopic fractionation is transient and represents an especially pronounced form of uphill diffusion.[61]

The profiles may be quantified by several metrics,[23] but the three of interest here are:

- F_{18}: net $^{18}O_i$ injection flux. The relationship between F_{18} and the total net flux F_{tot} of O_i (both isotopes) depends on the isotopic compositions of H_2O and dissolved O_2 as well as the chemical concentration of dissolved O_2. In the present case of dissolved air, F_{18} should be multiplied by a factor of 10.6 to obtain F_{tot}.[23]
- λ_1: characteristic length describing exponential decay at depths closely associated with uphill diffusion.
- λ_2: characteristic length describing exponential decay at depths well beyond those associated with uphill diffusion.

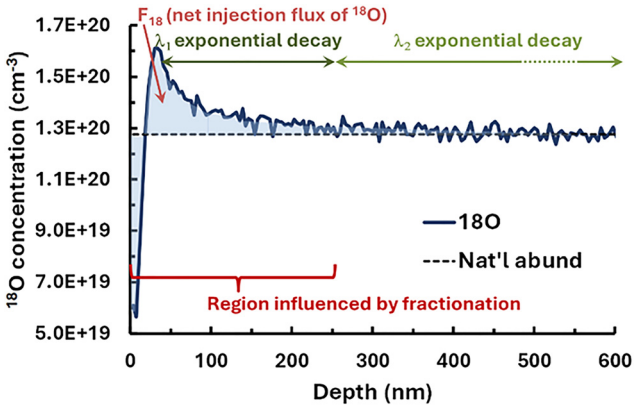

Fig. 1 Example ^{18}O profile illustrating the definition of the profile metrics F_{18}, λ_1 and λ_2. Profile was measured in air without UV illumination at 70 °C after 60 min diffusion. Potential bias applied was V_{appl} = −0.4 V *vs.* Ag/AgCl. The water (10 atomic % ^{18}O) contained no electrolyte, and was air-equilibrated prior to diffusion by bubbling for 10 min.

Ref. 23 details the fitting procedures used to obtain these metrics, with the primary features described in the SI. All features are stable during long-term storage. However, details of the profile shapes vary with position on a given specimen, and between specimens. Such variations have been discussed at length elsewhere[33,34] and arise mostly from differences in the level of surface contamination, especially adventitious carbon, which can poison the surface sites responsible for injection.

3.1 Effects of applied bias in the dark

As a reference point for UV studies, the empirical dependence of F_{18}, λ_1 and λ_2 on T and diffusion time t was measured with applied bias in the dark. Under such conditions, the governing physical processes entail breaking and forming of chemical bonds, both in fluid species (O_2, H_2O) and in adsorbed OH, and presumably have a corresponding Arrhenius-type temperature dependence. Accordingly, Fig. 2 shows Arrhenius plots of F_{18}, λ_1 and λ_2 from 30 ≤ T ≤ 70 °C. For comparison, Fig. 2 also shows data for these metrics without bias using a combination of previously published measurements,[23] new measurements obtained by the methods reported there, and the analysis procedure employed in the SI. The plots make clear that use of applied bias considerably increases the average values of all three metrics. Table T2 in the SI provides the effective activation energies of F_{18}, λ_1 and λ_2.

F_{18} depends upon the surface chemical processes of injection and annihilation. The wide variation in F_{18} at fixed temperature, often across the surface of a single specimen, results from variations in tiny concentrations of surface sites at which O_i injection is especially rapid.[34] Variability in semiconductor behavior mediated by small concentrations of surface sites has ample precedent. Procedures to minimize such variability in Si device fabrication took several decades to develop fully.[62] On TiO_2 single crystals, small concentrations of defects catalytically mediate much of the surface chemistry.[63] A general principle of heterogeneous catalysis is that the most reactive

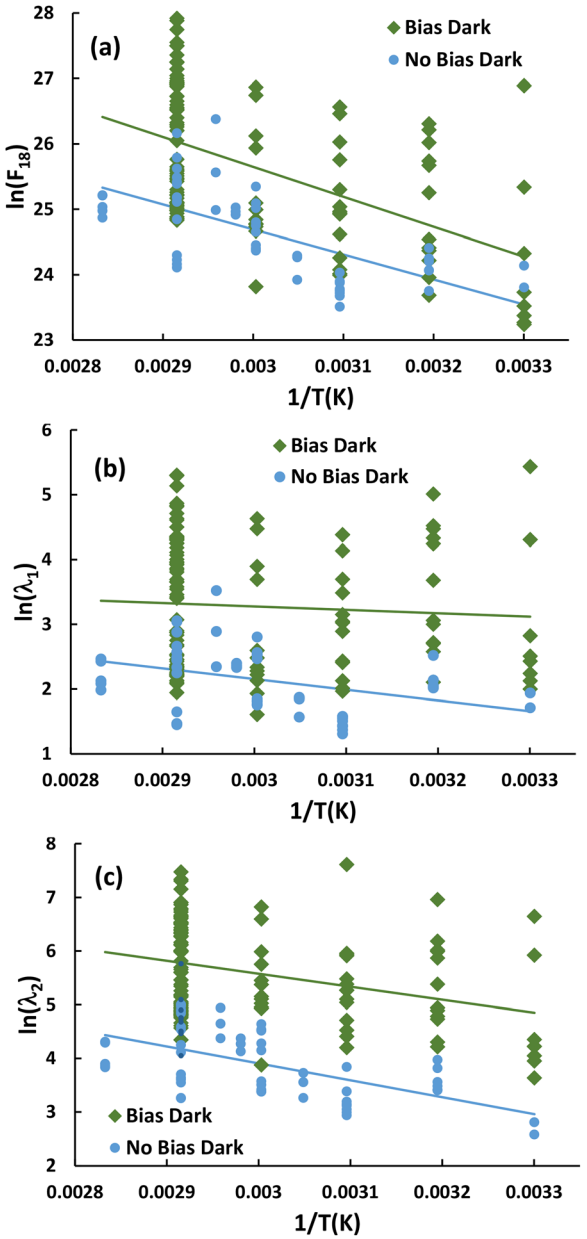

Fig. 2 Arrhenius plots for profile metrics under dark conditions with and without applied bias: (a) F_{18}, (b) λ_1 and (c) λ_2. Lines represent linear least squares fits.

surface sites are often most vulnerable to deactivation by poisoning.[64] Injection entails a form of catalysis wherein one reaction produce is O_i. Susceptibility to poisoning and the variability of injection rate that ensues[34] is therefore not surprising.

Fig. 2 also shows considerable variability for λ_1 and λ_2. These metrics are measured well within the bulk and depend directly upon bulk processes such as hopping diffusion, atom exchange with the lattice, and interstitial cluster formation.[23] However, progressive spatial and temporal evolution of clusters incorporating O_i provides a mechanism to couple bulk metrics to F_{18}.[34] Higher injection fluxes enable quicker evolution of the cluster isomer populations. Thus, much of the variability in λ_1 and λ_2 arises indirectly from the variations in F_{18}.

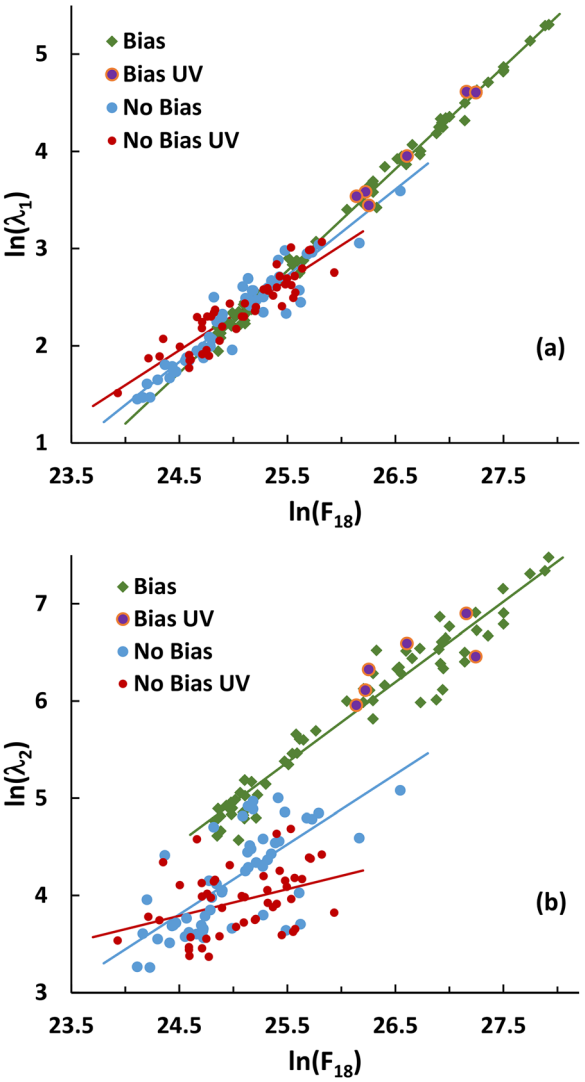

Fig. 3 Ln–ln plot of (a) λ_1 and (b) λ_2 *vs.* net injection flux F_{18} with and without applied bias, with and without UV illumination. Lines represent linear least squares fits of the points having corresponding color. No fit appears for applied bias with UV because too few points exist. All data shown with applied bias were measured at 70 °C. For λ_1 without bias, the general magnitudes of the points with and without UV are nearly identical, although the slopes differ slightly. For λ_2 without bias, UV illumination decreases λ_2 at higher values of F_{18}. The difference in slopes of the respective lines are statistically very significant. With bias, UV increases λ_2 but the effect is slight, requiring statistical analysis as described in the text to identify with confidence.

To quantify this coupling, Fig. 3 shows plots of λ_1 and λ_2 *vs.* F_{18} in ln–ln form. All metrics with applied bias (green points) were measured at 70 °C. The plots of both λ_1 and λ_2 *vs.* F_{18} show good linearity, signifying an empirical power law dependence. Table 1 lists the corresponding slopes m, which provide the exponents m for normalization of bulk metrics by F_{18}^m.

Fig. 3 also shows corresponding data for λ_1 and λ_2 (blue points) measured without applied bias using previously published results,[33] new measurements obtained by the methods reported there, and the analysis procedure employed in the SI.

Table 1 Values of m for normalization of metrics by F_{18}^m

Metric	Applied bias dark	Without bias dark	Without bias UV
λ_1	1.05 ± 0.01	0.89 ± 0.04	0.72 ± 0.05
λ_2	0.83 ± 0.02	0.72 ± 0.10	0.27 ± 0.10

However, fewer data were available at 70 °C than for measurements with applied bias. To compensate for the smaller data set, a scaling procedure was employed to remove the effects of differing T. The regression lines from the Arrhenius plots in Fig. 2 were used to estimate the value of each data point scaled to 70 °C. In a chosen Arrhenius plot this procedure in effect translates points at $T \neq 70$ °C parallel to the regression line to $T = 70$ °C – quantitatively preserving the standard error around the regression line. We have employed this procedure elsewhere,[33] but without a direct test of its validity. Here, such a test becomes possible using the data with applied bias because of the large number of points across the entire temperature range (about 125). When the entire data sets for λ_1 and λ_2 were scaled to 70 °C, the resulting lines changed slope by only a few percent. The scatter about the corresponding regression lines worsened, but only slightly. These results indicate that the scaling procedure does not introduce significant distortions or biases into the analysis.

Even after variability due to F_{18} is accounted for, Fig. 3's data for λ_1 and λ_2 without bias (both dark and UV) exhibit more scatter than the corresponding results with bias. The origin of this added scatter remains unclear at present, but procedural or metrological differences cannot explain it because the same equipment and methodology were employed for all data sets. However, an empirical linear correlation between $\ln(\lambda_1)$ and $\ln(F_{18})$ works very well for data with bias. We therefore employed similar empirical linear fitting for data without bias (both dark and UV) to create a basis for comparing all the data sets quantitatively. The slopes of λ_1 and λ_2 without bias in the dark (Table 1) fall somewhat below those with applied bias. However, the slopes for λ_2 fall within each other's error bars.

Experiments were performed to examine the time dependence of the three metrics with applied bias. Fig. 4a shows $\ln(F_{18})$ at 70 °C *vs.* $\ln(t)$ in the range 6–60 min. In this range, $\ln(F_{18})$ decreases with a slope of −0.90 ± 0.20. The decrease presumably originates from increasing back-diffusion and annihilation of O_i to the surface as the concentration of O_i in the bulk steadily increases. Surface annihilation is required by the principle of microscopic reversibility, as has been previously reported and discussed for O_i injection into metal oxides.[23]

Corresponding plots for λ_1 and λ_2 with bias at 70 °C appear in Fig. S3 of the SI. These metrics by themselves exhibit little time dependence. However, they are heavily convolved with the time dependence of F_{18} as discussed above. To examine the effects of time on profile evolution in these regions independent of F_{18}, Fig. 4 also shows ln–ln plots of $\lambda_1/F_{18}^{1.05}$ and $\lambda_2/F_{18}^{0.83}$ *vs.* t. Both normalized metrics increase with time. The slopes in Fig. 4 are 1.05 ± 0.04 for $\lambda_1/F_{18}^{1.05}$ and 0.78 ± 0.05 for $\lambda_2/F_{18}^{0.83}$.

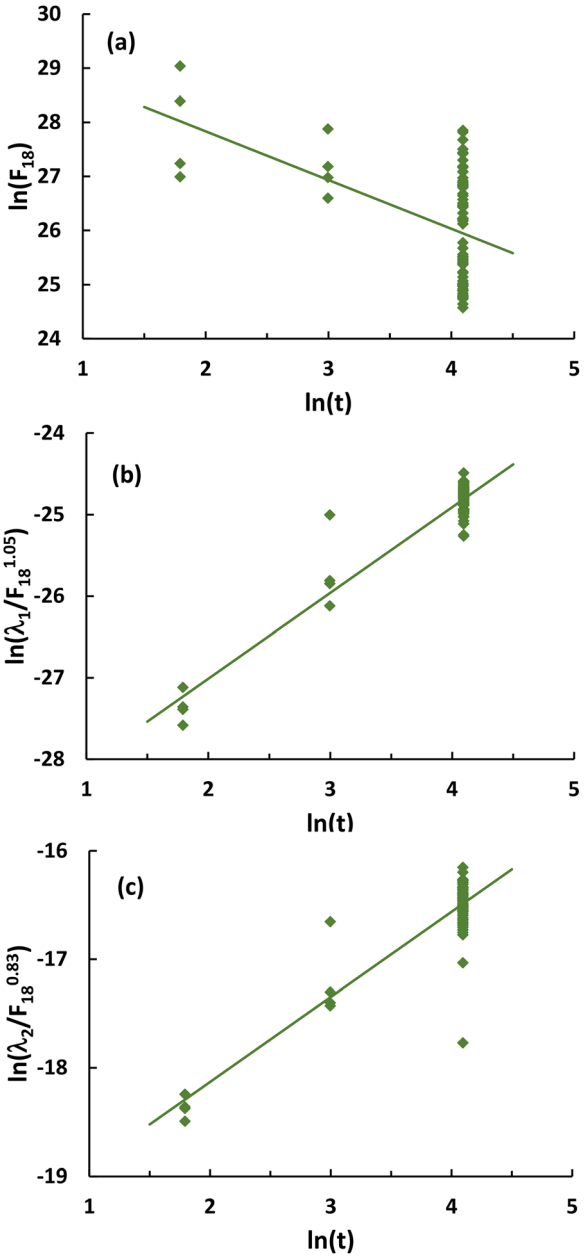

Fig. 4 Profile metrics *vs.* diffusion time t (min) at 70 °C for (a) $\ln(F_{18})$, (b) $\ln(\lambda_1/F_{18}^{1.05})$ and (c) $\ln(\lambda_2/F_{18}^{0.83})$. Lines represent linear least squares fits. Dense clustering near the line obscures many data points at $\ln(t)$ = 4.1 in (c) and especially in (b).

3.2 Effects of ultraviolet illumination

Fig. 5 shows Arrhenius plots of F_{18}, λ_1 and λ_2 without applied bias, both in the dark and with UV illumination. Table T2 in the SI provides the corresponding effective activation energies. The data shown in blue (measured in the dark) replicate the corresponding results in Fig. 2, with expanded vertical scales in Fig. 5 to enable clearer comparison with UV results. The effects of UV illumination on F_{18} and λ_1 broadly accord with those reported in a previous study[33] (wherein λ_1 was termed "λ"), with differences in detail arising from the enlarged data set and

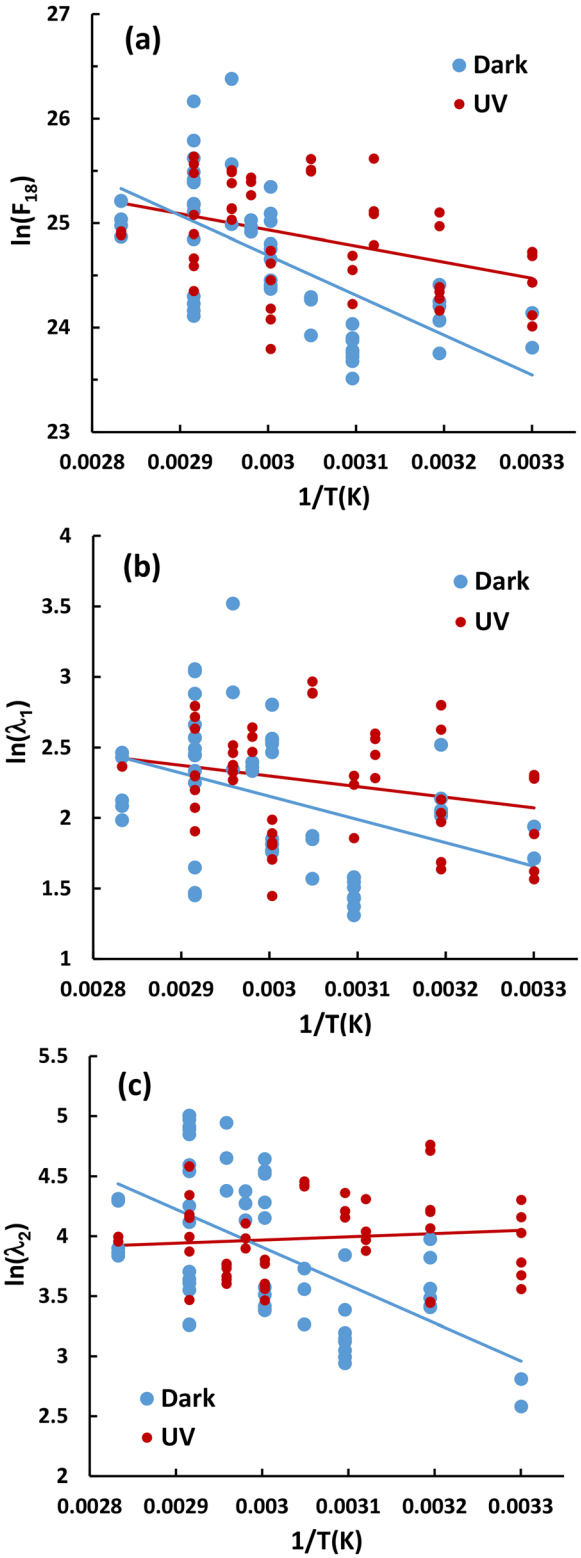

Fig. 5 Arrhenius plots for profile metrics under dark and UV conditions without applied bias: (a) F_{18}, (b) λ_1 and (c) λ_2. Lines represent linear least squares fits.

significant differences in the procedure for computing profile metrics. For example, existence of the λ_2 region was not known at the time of the previous study.

Thus, the UV data in Fig. 5 were scaled to 70 °C as described above for dark data and were plotted in Fig. 3 as red points with empirical linear fits. Table 1 shows the corresponding slopes. For λ_1, UV illumination exerts little effect on the general magnitude, but the slope m decreases noticeably. The ranges encompassed by the error bars with and without UV do not overlap. For λ_2, UV illumination dramatically decreases m, and the ranges encompassed by their respective standard deviations come nowhere near overlapping. Visually, the points at the high end of the flux range lie noticeably lower than the corresponding points measured in the dark.

The variability of λ_2, together with higher injection fluxes made possible by applied potential bias (increasing the signal-to-noise ratio for measuring λ_2), prompted measurement of additional data under UV illumination with bias. An elevated temperature of 70 °C was chosen because Fig. 2(c) shows that λ_2 increases with T. Although measurements are possible at 80 °C or higher, loss of labeled water to evaporation becomes a significant problem on the time scale of these experiments, even with refluxing.

Fig. 3 shows the results with points that are purple and orange. UV prompts no discernable change in λ_1. Surprisingly, UV appears to increase λ_2, although the effect is too small to assess its reliability with visual inspection alone. Statistical analysis is necessary.

Such analysis directly on F_{18}, λ_1 and λ_2 can be misleading, as all these metrics vary over ranges nearly two orders of magnitude wide. Histograms of the distributions[23] reveal significant deviations from normality in the form of strong positive skew. In addition, all three metrics are heteroscedastic (*i.e.*, the standard deviation varies with the value of the metric itself), which is common for data sets encompassing such wide ranges. Various methods have been proposed for reliable statistical analysis of heteroscedastic, non-normal data.

Logarithmic transformation is a common approach employed across a wide range of disciplines including biology,[65] chemistry,[66] epidemiology,[67] environmental science,[68,69] social science,[70] econometrics[71] and others. The transformation often removes heteroscedasticity and sometimes leads to normal distributions. Arrhenius plotting as in Fig. 2 requires logarithmic transformation. The distributions for all three metrics become homoscedastic after transformation.

However, the distributions continue to deviate from normality. Classical parametric statistical tests (*e.g.*, *t*-tests) exhibit considerable robustness to deviations from a normal distribution,[72,73] but reformulation of the variables based on independent knowledge of the physical system is preferable whenever possible.[65] Such a reformulation here is indeed possible as described above: determination of empirical exponents m for normalization of bulk metrics by F_{18}^m. For a given bulk metric, m represents an empirical quantity that depends upon t and several other processes occurring in the bulk. Nevertheless, for profiles measured with applied bias, histograms of the normalized metrics $\lambda_1/F_{18}^{1.05}$ and $\lambda_2/F_{18}^{0.83}$ follow normal distributions, indicating that the non-normality previously reported[23] for λ_1 and λ_2 was due to the influence of F_{18}.

Table 2 Normalized profile metrics and statistical results (with applied bias)[a]

	Mean (dark)	Mean (UV)	Deg of freedom	p_t	p_{MW}
$\ln(F_{18})$	26.0 ± 0.9	26.5 ± 0.5	8	0.053	0.20
$\lambda_1/F_{18}^{1.05}$	$(4.03 \pm 0.29) \times 10^{-11}$	$(4.14 \pm 0.32) \times 10^{-11}$	76	0.40	—
$\lambda_2/F_{18}^{0.83}$	$(1.19 \pm 0.24) \times 10^{-7}$	$(1.38 \pm 0.30) \times 10^{-7}$	76	0.069	—

[a] Two-tailed, equal variances (pooled) except for $\ln(F_{18})$, which assumes unequal variances.

Table 2 shows the means and standard deviations of $\ln(F_{18})$, $\lambda_1/F_{18}^{1.05}$ and $\lambda_2/F_{18}^{0.83}$. All these variables are homoscedastic. The latter two obey normal distributions, but $\ln(F_{18})$ does not. For completeness, Table T3 in the SI shows the means and standard deviations of the original metrics (F_{18}, λ_1 and λ_2) under both dark and UV conditions with applied bias at 70 °C. Because these variables are heteroscedastic and encompass ranges up to two orders of magnitude, their standard deviations look unnaturally large.

Table 2 also shows the results of *t*-tests comparing the values of $\ln(F_{18})$, λ_1/F_{18} and $\lambda_2/F_{18}^{0.8}$ with and without UV illumination. For both $\ln(F_{18})$ and $\lambda_2/F_{18}^{0.83}$, the likelihoods p_t are 0.07 or below that illumination has no statistically significant effect. In contrast, p_t is much larger at 0.4 for $\lambda_1/F_{18}^{1.05}$. In other words, UV probably increases λ_2 directly but exerts no direct effect on λ_1.

The *t*-test for $\ln(F_{18})$ is suspect because of the non-normal, positively skewed distribution. Distributions with strong positive skew tends to overestimate statistical significance in *t*-tests.[74] Thus, a non-parametric Mann–Whitney *U*-test was also applied to $\ln(F_{18})$ that does not presuppose normality. The non-parametric test effectively compares medians[75] rather than means. Compared to a *t*-test, a Mann–Whitney test is less vulnerable to type I errors that reject the null hypothesis when it is true. The resulting probability p_{MW} is 0.20. However, a Mann–Whitney test is more vulnerable than a *t*-test to type II errors that fail to reject the null hypothesis when it is false.

The statistical tests for $\ln(F_{18})$ thus provide a mixed assessment. The *t*-test implies strong statistical significance, while the Mann–Whitney test implies much weaker significance. However, both tests suffer drawbacks. As suggested by Fig. 5a without bias, the effect of UV varies with T and may be too small at 70 °C to reliably detect given the variability in the data sets.

A few crystals that were diffused with applied bias were subjected to progressive annealing steps between 100 and 300 °C. In contrast to previous work without applied bias,[12] wherein such heating induced appreciable profile spreading, the profiles generated with bias exhibited no measurable spreading up to and including 300 °C.

3.3 DFT results for clusters of O_i and H_i

Fig. S4 in the SI shows the defect formation energies computed *via* eqn (1) for the simple point defects O_i, V_O, H_i, and H_O, where H_O represents an H atom that substitutes for O in the TiO_2 lattice. For the O-related defects under O-rich conditions,

O_i is more stable than V_O for n-type material (nearly universal for TiO_2 single crystals). The ordering inverts for p-type material. In agreement with published studies,[21,52,76] O_i exists in the 2− charge state over much of the E_F range, and V_O in the 2+ charge state.[77,78] H_i exists primarily as a 1+ donor, in agreement with previous work.[13,17,79–82] H_O exists primarily as a 1+ donor, changing to a 1− acceptor at E_F close to the conduction band minimum (CBM). The donor behavior largely agrees with a previous study[80] that reported H_O to be exclusively a donor over the entire range of E_F A different study reported only acceptor behavior,[79] but that work placed E_F in the conduction band, and a full analysis of charge state *vs.* E_F was not performed. H_O is known to be amphoteric in other oxides such as ZnO,[83–85] and to a modest extent that behavior appears in Fig. S4.

For dimer clusters having stoichiometry O_i–H_i, the DFT calculations identified several isomers. This study did not attempt an exhaustive search of configuration space, but a random sampling method was employed to generate O_i–H_i defects. An O atom with randomly sampled spatial coordinates was placed within a single unit cell of the 3 × 3 × 4 TiO_2 supercell. An H atom was then placed within an annular region centered on the O defect, with the O–H distance drawn from a Gaussian distribution and the orientation determined by a randomly selected angle. The defective supercells then underwent geometry relaxation to determine the corresponding energies.

Fig. 6 shows the four most stable dimer cluster configurations, and Fig. S5a shows the corresponding formation energies. Dimer *a* exhibits exclusively donor behavior until it nears the conduction band edge, maintaining a constant charge state of 1+ for $E_F < 2.8$ eV, whereafter it exhibits acceptor behavior with a charge state of 2−. Dimers *b*–*d* adopt various forms of a split geometry, which means that the two O atoms associated with a single lattice site form no chemical bond between each other. These isomers are 1− and 3− acceptors for $E_F > 0.8$ eV but become neutral for E_F lower in the bandgap. From the thermodynamic perspective of formation energies, dimer *a* is most stable for $0 < E_F < 1.7$ eV, and dimer *b* dominates for $E_F > 1.7$ eV. Dimers *c* and *d* are never the most stable species; *c* and *d* formation energies are 0.5–0.6 eV larger than that of *b* throughout the entire band gap. From the kinetic perspective, the situation could differ as detailed in the Discussion. Notably, the H atoms in dimers *b* and *c* bond directly to one of the O atoms comprising the defect's O_i "core." In dimers *a* and *b*, the H atom forms the strongest bond to O atoms neighboring the defect core.

For trimer clusters of interstitials having stoichiometry O_i–$(H_i)_2$, the DFT calculations again identified several isomers. Fig. 7 shows the five most stable configurations, and Fig. S5b shows the corresponding formation energies. Trimers *a*, *d* and *e* are donors, with *a* and *d* maintaining 2+ charge for all E_F and *e* maintaining 1+. Trimer *c* is neutral for all E_F up to 2.8 eV, whereafter it transitions through charge states 2−, 3−, 4−, and 5− for $E_F > 2.8$ eV. Trimer *b* is neutral for $E_F < 1.0$ eV, a 2− acceptor for $1.0 < E_F < 2.8$ eV and transitions through charge states 1−, 2−, 3−, 4−, and 5− for $E_F > 2.8$ eV. As with dimers, the geometries of these trimers remain largely unchanged regardless of their charge state. From a thermodynamic perspective of formation energies, dimer *a* is most stable for $0 < E_F < 2.0$ eV. Trimer *c* dominates for a narrow range $2.0 < E_F < 2.5$ eV and trimer *b* dominates for $E_F > 2.5$ eV, Trimers *d* and *e* are never the most stable species. The connection between stability and bonding of H differs from that of dimers. For trimers, only *a* has no H atoms bonded directly to the O atoms in the core O_i defect. In *d* and *e*, one H atom bonds to the core defect, while in *b* and *c*, both H atoms bond to core O atoms.

As noted in the Methods section, H and to a lesser extent O were not fully in contact with an external reservoir of the corresponding elements. Under such kinetically limited

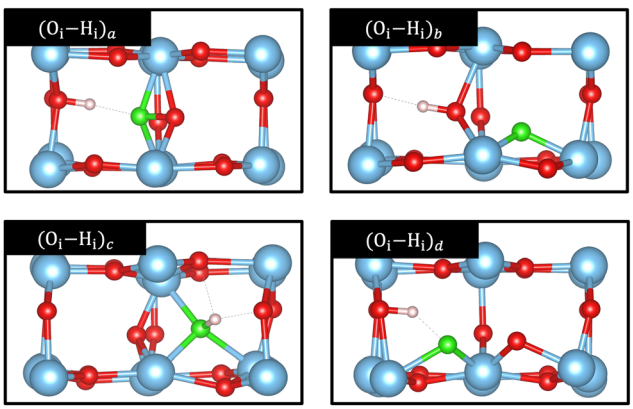

Fig. 6 Geometries of the four most stable dimers O_i–H_i. Blue, white and red spheres respectively represent Ti, lattice O and H. Green signifies the "extra" O in the core O interstitial.

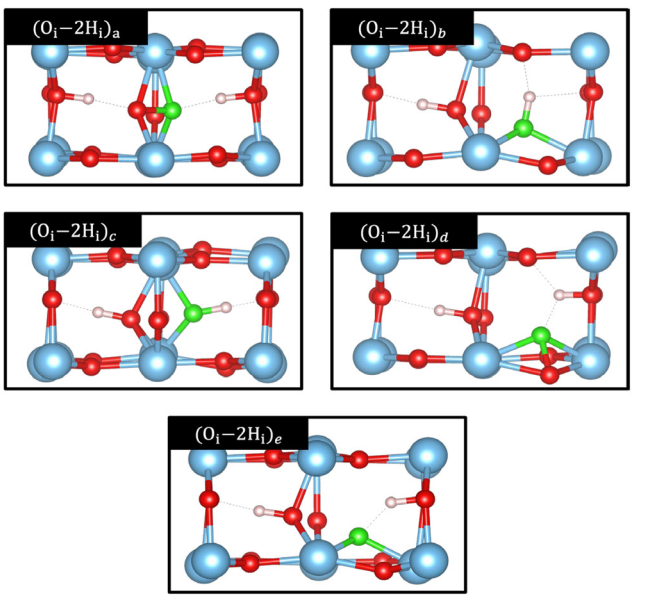

Fig. 7 Geometries of the five most stable trimers O_i–$(H_i)_2$. Blue, white and red spheres respectively represent Ti, lattice O and H. Green signifies the "extra" O in the core O interstitial.

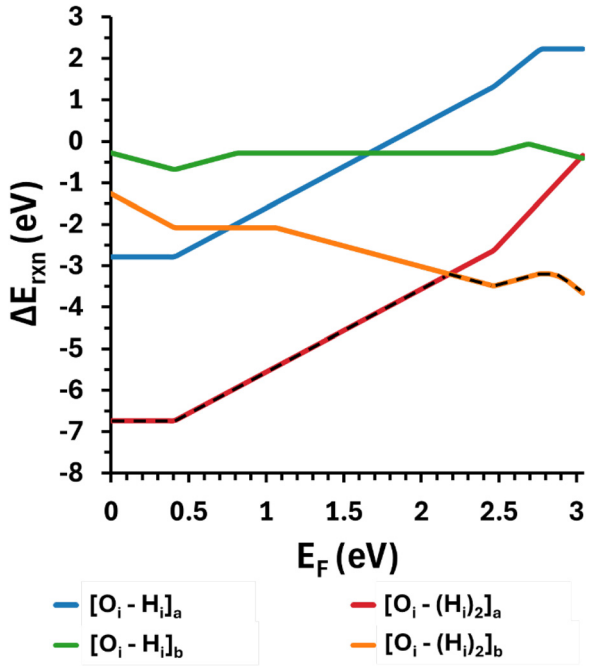

Fig. 8 Reaction energies of selected interstitial dimers and trimers that form exothermically from their constituent point defects over most of the range of E_F. Identity of the most exothermic isomer varies with E_F and is traced with dashed lines.

conditions, it is more appropriate to gauge the propensity to form dimer and trimer species *via* their reaction energies (ΔE_{rxn}) with respect to the reactants O_i and H_i. Exothermic reactions with $\Delta E_{rxn} < 0$ are more likely to occur than endothermic reactions.

Accordingly, Fig. 8 shows ΔE_{rxn} *vs.* E_F for the dimers and trimers described above exhibiting the most negative values of ΔE_{rxn}. The details of the plots are complicated, but the high-level conclusion is that, over the entire range of E_F, at least one dimer and one trimer exist for which formation from O_i and H_i is exothermic. For completeness, Fig. S6a and b depict ΔE_{rxn} *vs.* E_F for all dimers and trimers, respectively.

4. Discussion

Most literature describing the effects of photostimulation on defect-mediated diffusion focuses on the formation energies of mobile charged defects.[27,86,87] Photogenerated minority carriers affect these energies, which propagate into mobile defect concentrations and the corresponding effective diffusivities. The effects on hopping are usually not considered unless the dominant charge state changes (and thereby the relevant hopping barrier)[88,89] or direct conversion of electronic to vibrational energy at the defect induces hopping.[8] However, thermodynamic formation energies have little relevance in the present kinetically limited system. Effects of interstitial hopping and clustering are more important.

The lack of knowledge about interstitial cluster formation in oxides near room temperature probably reflects their substantial mobility,[13,90] which enables their rapid capture by bulk traps or surfaces. Interstitial clustering behavior near room temperature has started to attract attention only recently, and mainly in Si-based systems[9] where illumination exerts noticeable effects.

An important experimental complication compounds the lack of knowledge; super-bandgap illumination is absorbed and ultimately converted into heat. Thus, illumination may simultaneously induce both thermal and nonthermal effects that are difficult to disaggregate.[89] Keeping the illumination intensity low minimizes such effects, and an important aspect of the present data rules out this complication here. The effective activation energy of F_{18} is higher than that of λ_2, implying that F_{18} has a stronger temperature dependence. Yet λ_2 in Table 1 shows a greater fractional increase in response to UV than F_{18}. Heating alone would result in F_{18} exhibiting the larger fractional increase.

4.1 Response of the profile metrics to UV

Fig. 3 and 4 show that F_{18}, λ_1 and λ_2 all change in different ways in response to applied bias, t and UV illumination. These trends all point to differences in the primary governing mechanism for each metric.

Little theory exists for λ_1, which contains ^{18}O that has diffused from the "valley" region of isotopic fractionation.[22] However, the λ_1 region is much closer to the surface than the λ_2 region. Therefore, the λ_1 develops sooner than the λ_2 region, and the concentration of O_i at any given time is higher. For these reasons, the λ_1 region responds less to trapping effects than the λ_2 region. If trapping effects are weak, the normalized metric λ_1/F_{18}^m depends primarily upon the diffusivity D. As mentioned above, there is precedent for super-bandgap illumination to affect the interstitial hopping barrier[88,89] due to a change in the majority charge state. However, this effect seems to be either small or nonexistent here, both with and without applied bias.

In contrast, λ_2 samples a region far deeper in the solid, which is exposed to lower concentrations of O_i for shorter times. A metric measured in this region is more sensitive to the effects of small concentrations of saturable O_i traps. D probably affects λ_2, but photostimulated effects on D appear to be negligible. With possible effects of UV on F_{18} removed from the normalized variable, the evidence points to significant changes in λ_2 due to UV, corresponding to modified O_i capture by traps.

F_{18} contains primarily surface rate parameters as well as the coverage of injectable O, which is presumably set by liquid–surface interactions. As mentioned in the Methods, the application of bias may remove dissolved impurities that poison injection sites with high activity. Also, the electrodes and associated wiring may unintentionally introduce to the liquid small amounts of impurities such as Na. Ions of Na have recently been shown[91] to shed their hydration shell and bond directly to TiO_2(110), thereby setting up very strong electric fields (10^8 V cm^{-1}) that could influence the injection of charged species such as O_i.

Although surface kinetic parameters dominate F_{18}, it also contains *D via* the surface annihilation rate. Thus, UV can affect F_{18} directly *via* the surface rate parameters and indirectly *via D*. Here, however, UV exerts little if any influence on *D*.

Without applied bias, UV increases F_{18} (Fig. 2a), at the lower end of the temperature range. UV exerts little effect at 70 °C, a finding consistent with the mixed statistical results (Mann–Whitney and *t*-tests) discussed above with applied bias. This study cannot determine why UV increases F_{18} at lower temperatures, although removal of carbonaceous impurities by photo-oxidation has been proposed to cause UV-induced increases in hydrophilicity on TiO_2(110).[92] A similar mechanism may clear O_i injection sites of carbonaceous poisons.

4.2 Properties of interstitial clusters

O_i and H_i are known to form clusters when both species are extrinsic to the semiconductor, as in Si.[93] In metal oxides, progressive annealing measurements[12] of ^{18}O profiles after aqueous submersion of TiO_2 and ZnO single crystals have suggested that families of $(O_i)_y$–$(H_i)_x$ interstitial clusters immobilize O_i, but supporting computational evidence was lacking. The DFT calculations detailed in this work provide such evidence.

Interstitial families of clusters exist for dopants in silicon, such as boron.[94] In UO_2, wherein the U cation and O anion have comparable sizes, ''Willis clusters'' containing multiple O_i atoms exist[95] along with mixed interstitial clusters containing O_i and H_i.[96] Thus, the identification of dimers and trimers containing O_i and H_i by the present calculations is not surprising. However, given the rarity of O_i in oxides not synthesized specifically to be hyperstoichiometric,[97,98] the behavior of O_i-containing clusters in oxides remains little investigated.

Certain aspects of the behavior observed here are straightforward to rationalize. The dominant charge states of the most thermodynamically stable dimers often represent the sums of the dominant charge states of the constituent O_i and H_i. The geometry of the dimer O_i core (dumbbell or split) mimics that of the parent O_i reactant. For trimers, the same patterns also hold for the most thermodynamically stable species except in highly n-type material, for which a split acceptor trimer exists. Typically, the most thermodynamically stable dimers and trimers isomerize to different geometries when changing ionization states – much like O_i does.

The dimer and trimer isomers differ considerably among themselves in geometry. The interconversion barriers were not examined but could be considerable given the rearrangements involved. Under kinetically controlled conditions near room temperature, thermodynamically unstable clusters may survive intact. The exothermicity of certain species in Fig. 8 are not helpful for predicting such isomerization; some of the depicted reactions are very exothermic in p-type material because the O_i reactant is very unstable thermodynamically under those conditions.

4.3 Effects of interstitial clustering

Traps for O_i in as-received rutile TiO_2 take several forms at submersion temperatures, including V_O, extended defects, and families[12,99,100] of small interstitial clusters. Hydrogen is ubiquitous in metal oxides[101,102] as an adventitious impurity and forms complexes with various defects,[102,103] including electron acceptors[101] such as O_i. The wide range of activation barriers that characterizes dissociation of O_i traps in TiO_2 suggests that the $(O_i)_x$–$(H_i)_y$ family of clusters may include many members. One isomer of the dimer has been reported previously[13] but the DFT results presented here show that several isomers of the dimer O_i–H_i and trimer O_i–$(H_i)_2$ may also form exothermically from O_i and H_i.

H_i may be produced if O_i replaces H_O in the lattice *via* a standard lattice kickout reaction, which seems likely. O_i may also react with molecular H_2 trapped in the lattice. H_2 has not been positively identified in rutile, although H_2 has been reported likely to exist in anatase.[104] Assuming H_2 exists in rutile, reaction with O_i would presumably lead to either O_i–$(H_i)_2$ or O_i–H_i plus free H_i. Clusters involving multiple O_i species may exist, but that possibility was not investigated here.

Some of the available traps for O_i, such as V_O and H_O substituting for O in the lattice,[79,83,105] can be saturated if exposed to enough O_i. The ability of clusters with the general formula $(O_i)_x$–$(H_i)_y$ to saturate remains unclear because many family members have not yet been identified. Saturable traps for O_i affect the λ_2 region most strongly where isotopic label concentrations remain close to natural abundance near the leading edge of the tail.

Smaller values of λ_2 imply more trapping. The correspondence suggests that in the absence of applied bias, UV increases the concentration of one or more small clusters containing O that absorb O_i. The effect is larger in the higher ranges of injection fluxes characteristic observed without bias. Candidate clusters include the O_i–H_i^- cluster as well as larger clusters of formula $(O_i)_y$–$(H_i)_x$ for which O_i–H_i^- serves as a kinetic precursor.

The primary cluster isomers identified in the DFT calculations exist in multiple charge states. This is probably also true of other isomers not yet identified. In the dark, the relative populations of the isomers and their charge states depend upon E_F. Under illumination, both the isomeric makeup and the charge states change depend on the isomers' and point defects' interactions with excess minority carriers *via* cross sections for carrier capture, excited state lifetimes, and other factors. The isomeric makeup can change by several pathways. One or more isomers' stability may increase or decrease due to altered charge state. The charge state of O_i or H_i may change, affecting the exothermicity of the formation reaction of one or more isomers. The concentration of H_i may change because its rate of formation from H_O or H_2 may depend upon the charge state of O_i or H_O. In other words, illumination alters the rate constants for formation or dissociation of $(O_i)_y$–$(H_i)_x$ or changes the concentration of the reactant H_i. Fig. 9a and b depict these ideas schematically.

With applied bias, F_{18} is larger than for any of the experiments without applied bias. The $(O_i)_y$–$(H_i)_x$ clusters are therefore more evolved and have a different balance of stoichiometries. This evolution is clear from the lack of spreading in progressive annealing experiments up to 300 °C, for which a

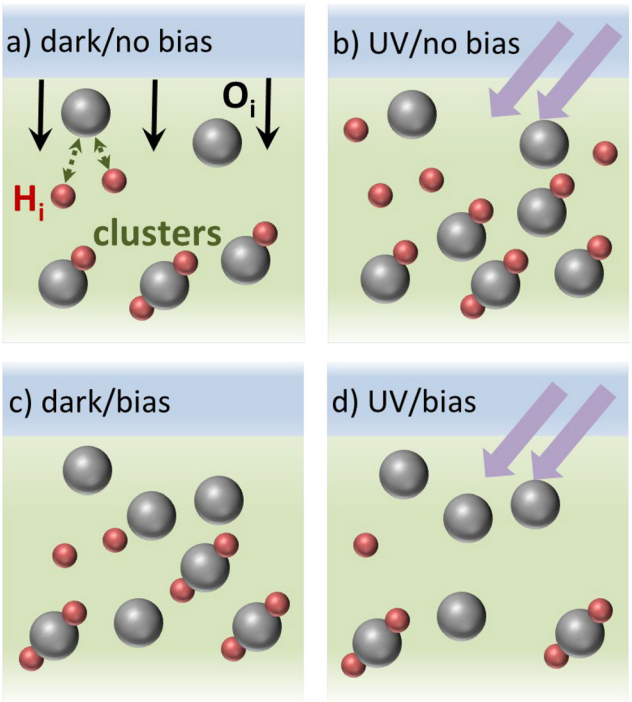

Fig. 9 Schematic depiction of the effects of UV illumination on interstitial clusters. Blue shading near the top of each panel represents the aqueous liquid. The surface of the green-shaded solid injects O_i (grey spheres) into the solid (shown by black arrows in (a)). O_i can then react (green arrows in (a) with H_i (red spheres) liberated from various forms of adventitious hydrogen already present in the solid to yield $(O_i)_y$–$(H_i)_x$ dimers, trimers, and perhaps higher-order clusters. UV illumination (b) decreases λ_2 by increasing the concentration of cluster traps for O_i by directly stabilizing the clusters and/or facilitating H_i creation. Panel (b) illustrates both effects. Application of potential bias (c) increases the rate of O_i injection. This increases the O_i concentration, which enables O_i to penetrate deeper, increasing λ_2. Faster injection also accelerates the evolution of cluster isomers (represented in (c) by an increase in the proportion of trimers to dimers). UV illumination acts on one or more isomers in this changed population (d) to decrease the concentration of cluster traps for O_i, thereby increasing λ_2 instead of decreasing it as in (b).

great deal of spreading occurs when diffusion occurs without applied bias. The lack of measurable spreading implies that few clusters have dissociated to release the O_i required for spreading. Fig. 9c illustrates this evolution schematically. The concentration of the preponderant cluster in this different population evidently decreases in response to UV illumination as depicted in Fig. 9d, leading to behavior of λ_2 that is opposite to illumination without bias wherein the preponderant cluster concentration increases in response to UV.

5. Conclusion

This study combines simulations of O_i–H_i clusters by density functional theory (DFT) with self-diffusion measurements of ^{18}O in submerged single-crystal rutile TiO_2(110) illuminated by ultraviolet (UV) light. The simulations show that O_i–$(H_i)_x$ dimers and trimers exist in several stable isomers, and each has multiple charge states that can change upon illumination. The diffusion measurements indicate that UV affects the concentration of interstitial clusters containing O_i, which changes the characteristic decay length for penetration of ^{18}O into the solid. Together, the simulations and experiments suggest that illumination alters the rate constants for formation or dissociation of $(O_i)_y$–$(H_i)_x$ or changes the concentration of the reactant H_i.

At a high level, this work introduces methods to facilitate kinetically dominated phenomena like strong isotopic fractionation by using submersion-created interstitials from oxide surfaces at temperatures below 100 °C. An important step has been taken to solidify the idea that families of interstitial clusters such as $(O_i)_y$–$(H_i)_x$ exist that can immobilize interstitials, and that coordination of temperature and illumination should enable their optimization for defect control.

Conflicts of interest

There are no conflicts of interest to declare.

Data availability

The data that support the findings of this study are included within the article and its supplementary information (SI). Supplementary information: summary method for determination of profile metrics; supplementary figures and tables. See DOI: https://doi.org/10.1039/d5cp04013b.

Acknowledgements

This work was supported by the U.S. National Science Foundation under grant DMR 17-09327 and DMR 23-22121, and the Air Force Office of Scientific Research under grant FA9550-21-0078. SIMS and XPS measurements were performed in the Materials Research Laboratory Central Research Facilities, University of Illinois at Urbana-Champaign. This work used PSC Bridges-2 at the Pittsburgh Supercomputing Center through allocation MAT220011 from the Advanced Cyberinfrastructure Coordination Ecosystem: Services and Support (ACCESS) program, which is supported by the National Science Foundation Grants No. 2138259, No. 2138286, No. 2138307, No. 2137603, and No. 2138296. The authors thank Jaeyoung Hong, Hexi Huang and Andros Gao for extensive help with performing the progressive annealing experiments.

References

1 H. Roth, W. Bernard, P. Zeldes and A. P. Schmid, Voltage-Annealing of Radiation Damage in Tunnel Diodes, *J. Appl. Phys.*, 1963, **34**, 669–671.
2 D. Macdonald, F. Rougieux, A. Cuevas, B. Lim, J. Schmidt, M. Di Sabatino and L. J. Geerligs, Light-induced boron-oxygen defect generation in compensated p-type Czochralski silicon, *J. Appl. Phys.*, 2009, **105**, 093704.

3 F. Fertig, R. Lantzsch, F. Frühauf, F. Kersten, M. Schütze, C. Taubitz, J. Lindroos and J. W. Müller, Excessive light-induced degradation in boron-doped Cz silicon PERC triggered by dark annealing, *Sol. Energy Mater. Sol. Cells*, 2019, **200**, 109968.
4 Y.-C. Zhao, W.-K. Zhou, X. Zhou, K.-H. Liu, D.-P. Yu and Q. Zhao, Quantification of light-enhanced ionic transport in lead iodide perovskite thin films and its solar cell applications, *Light: Sci. Appl.*, 2017, **6**, e16243.
5 G. Y. Kim, A. Senocrate, T.-Y. Yang, G. Gregori, M. Grätzel and J. Maier, Large tunable photoeffect on ion conduction in halide perovskites and implications for photodecomposition, *Nat. Mater.*, 2018, **17**, 445–449.
6 D. V. Lang and L. C. Kimerling, Observation of Recombination-Enhanced Defect Reactions in Semiconductors, *Phys. Rev. Lett.*, 1974, **33**, 489–492.
7 E. Mosconi, D. Meggiolaro, H. J. Snaith, S. D. Stranks and F. De Angelis, Light-induced annihilation of Frenkel defects in organo-lead halide perovskites, *Energy Environ. Sci.*, 2016, **9**, 3180–3187.
8 J. D. Weeks, J. C. Tully and L. C. Kimerling, Theory of recombination-enhanced defect reactions in semiconductors, *Phys. Rev. B*, 1975, **12**, 3286–3292.
9 J. Coutinho, D. Gomes, V. J. B. Torres, T. O. Abdul Fattah, V. P. Markevich and A. R. Peaker, Theory of reactions between hydrogen and group-III acceptors in silicon, *Phys. Rev. B*, 2023, **108**, 14111.
10 M. Siebenhofer, A. Viernstein, M. Morgenbesser, J. Fleig and M. Kubicek, Photoinduced electronic and ionic effects in strontium titanate, *Mater. Adv.*, 2021, **2**, 7583–7619.
11 M. Lyulyukin, N. Kovalevskiy, I. Prosvirin, D. Selishchev and D. Kozlov, Thermo-photoactivity of pristine and modified titania photocatalysts under UV and blue light, *J. Photochem. Photobiol., A*, 2022, **425**, 113675.
12 H. Jeong and E. G. Seebauer, Influence of interstitial cluster families on post-synthesis defect manipulation and purification of oxides using submerged surfaces, *J. Chem. Phys.*, 2024, **161**, 121103.
13 H. Jeong, E. Ertekin and E. G. Seebauer, Surface-Based Post-synthesis Manipulation of Point Defects in Metal Oxides Using Liquid Water, *ACS Appl. Mater. Interfaces*, 2022, **14**, 34059–34068.
14 A. Janotti and C. G. Van de Walle, Hydrogen multicentre bonds, *Nat. Mater.*, 2007, **6**, 44–47.
15 H. Li and J. Robertson, Behaviour of hydrogen in wide band gap oxides, *J. Appl. Phys.*, 2014, **115**, 203708.
16 A. Venzie, A. Portoff, E. C. P. Valenzuela, M. Stavola, W. B. Fowler, S. J. Pearton and E. R. Glaser, Impurity-hydrogen complexes in β-Ga2O3: Hydrogenation of shallow donors *vs.* deep acceptors, *J. Appl. Phys.*, 2022, **131**, 035706.
17 A. J. Hupfer, E. V. Monakhov, B. G. Svensson, I. Chaplygin and E. V. Lavrov, Hydrogen motion in rutile TiO2, *Sci. Rep.*, 2017, **7**, 17065.
18 M. D. McCluskey, M. C. Tarun and S. T. Teklemichael, Hydrogen in oxide semiconductors, *J. Mater. Res.*, 2012, **27**, 2190–2198.
19 Y. Knausgård Hommedal, M. Etzelmüller Bathen, V. Mari Reinertsen, K. Magnus Johansen, L. Vines and Y. Kalmann Frodason, Theoretical modeling of defect diffusion in wide bandgap semiconductors, *J. Appl. Phys.*, 2024, **135**, 170902.
20 H. Jeong, M. Li, J. Kuang, E. Ertekin and E. G. Seebauer, Mechanism of Creation and Destruction of Oxygen Interstitial Atoms by Nonpolar Zinc Oxide(10-10) Surfaces, *Phys. Chem. Chem. Phys.*, 2021, **23**, 16423–16435.
21 H. Jeong, E. Ertekin and E. G. Seebauer, Kinetic Control of Oxygen Interstitial Interaction with TiO2(110) *via* the Surface Fermi Energy, *Langmuir*, 2020, **36**, 12632–12648.
22 H. Jeong and E. G. Seebauer, Strong Isotopic Fractionation of Oxygen in TiO2 Obtained by Surface-Enhanced Solid-State Diffusion, *J. Phys. Chem. Lett.*, 2022, **13**, 9841–9847.
23 H. Jeong, I. I. Suni, R. Chen, M. Miletic, X. Su and E. G. Seebauer, Reactions of fluid and lattice oxygen mediated by interstitial atoms at the TiO2(110)–water interface, *Phys. Chem. Chem. Phys.*, 2025, **27**, 9522–9536.
24 J. Wang, R. C. Ewing and U. Becker, Average structure and local configuration of excess oxygen in UO2 + x, *Sci. Rep.*, 2014, **4**, 4216.
25 D. A. Andersson, T. Watanabe, C. Deo and B. P. Uberuaga, Role of di-interstitial clusters in oxygen transport in UO2 + x from first principles, *Phys. Rev. B:Condens. Matter Mater. Phys.*, 2009, **80**, 60101.
26 Z. Zhang and A. Janotti, Cause of Extremely Long-Lasting Room-Temperature Persistent Photoconductivity in $SrTiO_3$ and Related Materials, *Phys. Rev. Lett.*, 2020, **125**, 126404.
27 K. Alberi and M. A. Scarpulla, Suppression of compensating native defect formation during semiconductor processing *via* excess carriers, *Sci. Rep.*, 2016, **6**, 27954.
28 X. Xie, B. Li, Z. Zhang, S. Wang and D. Shen, Controlled compensation *via* non-equilibrium electrons in ZnO, *Sci. Rep.*, 2018, **8**, 17020.
29 A. Klump, M. P. Hoffmann, F. Kaess, J. Tweedie, P. Reddy, R. Kirste, Z. Sitar and R. Collazo, Control of passivation and compensation in Mg-doped GaN by defect quasi Fermi level control, *J. Appl. Phys.*, 2020, **127**, 045702.
30 B. Hammann, P. Vieira Rodrigues, N. Aßmann, W. Kwapil, F. Schindler, M. C. Schubert and S. W. Glunz, Deciphering the Role of Hydrogen in the Degradation of Silicon Solar Cells under Light and Elevated Temperature, *Sol. RRL*, 2024, **8**, 2400457.
31 D. Rana, S. Agarwal, M. Islam, A. Banerjee, B. P. Uberuaga, P. Saadatkia, P. Dulal, N. Adhikari, M. Butterling, M. O. Liedke, A. Wagner and F. A. Selim, Light-driven permanent transition from insulator to conductor, *Phys. Rev. B*, 2021, **104**, 245208.
32 A. Viernstein, M. Kubicek, M. Morgenbesser, T. M. Huber, E. Ellmeyer, M. Siebenhofer, C. A. F. Vaz and J. Fleig, Mechanism of photo-ionic stoichiometry changes in SrTiO3, *Solid State Ionics*, 2022, **383**, 115992.
33 H. Jeong and E. G. Seebauer, Effects of Ultraviolet Illumination on Oxygen Interstitial Injection from TiO2 under Liquid Water, *J. Phys. Chem. C*, 2022, **126**, 20800–20806.

34 H. Jeong and E. G. Seebauer, Effects of adventitious impurity adsorption on oxygen interstitial injection rates from submerged TiO 2 (110) and ZnO(0001) surfaces, *J. Vac. Sci. Technol., A*, 2023, **41**, 033203.
35 J. Zhang, S. Ferrie, S. Zhang, Y. B. Vogel, C. R. Peiris, N. Darwish and S. Ciampi, Single-Electrode Electrochemistry: Chemically Engineering Surface Adhesion and Hardness To Maximize Redox Work Extracted from Tribocharged Silicon, *ACS Appl. Nano Mater.*, 2019, **2**, 7230–7236.
36 C. Liu and A. J. Bard, Electrons on dielectrics and contact electrification, *Chem. Phys. Lett.*, 2009, **480**, 145–156.
37 P. Hohenberg and W. Kohn, Inhomogeneous Electron Gas, *Phys. Rev.*, 1964, **136**, B864–B871.
38 W. Kohn and L. J. Sham, Self-Consistent Equations Including Exchange and Correlation Effects, *Phys. Rev.*, 1965, **140**, A1133–A1138.
39 G. Kresse and D. Joubert, From ultrasoft pseudopotentials to the projector augmented-wave method, *Phys. Rev. B: Condens. Matter Mater. Phys.*, 1999, **59**, 1758–1775.
40 P. E. Blöchl, Projector augmented-wave method, *Phys. Rev. B:Condens. Matter Mater. Phys.*, 1994, **50**, 17953–17979.
41 G. Kresse and J. Furthmüller, Efficient iterative schemes for ab initio total-energy calculations using a plane-wave basis set, *Phys. Rev. B:Condens. Matter Mater. Phys.*, 1996, **54**, 11169–11186.
42 G. Kresse and J. Furthmüller, Efficiency of ab-initio total energy calculations for metals and semiconductors using a plane-wave basis set, *Comput. Mater. Sci.*, 1996, **6**, 15–50.
43 J. P. Perdew, K. Burke and M. Ernzerhof, Generalized Gradient Approximation Made Simple, *Phys. Rev. Lett.*, 1996, **77**, 3865–3868.
44 G. C. Vásquez, S. Zh Karazhanov, D. Maestre, A. Cremades, J. Piqueras and S. E. Foss, Oxygen vacancy related distortions in rutile TiO_2 nanoparticles: A combined experimental and theoretical study, *Phys. Rev. B*, 2016, **94**, 235209.
45 A. Janotti, J. B. Varley, P. Rinke, N. Umezawa, G. Kresse and C. G. Van de Walle, Hybrid functional studies of the oxygen vacancy in TiO2, *Phys. Rev. B:Condens. Matter Mater. Phys.*, 2010, **81**, 85212.
46 Y.-S. Kim, Y.-C. Chung and K. S. Lee, The electronic structure of Ni doped rutile TiO2, *J. Electroceram.*, 2006, **17**, 951–953.
47 K. V. K. Rao, S. V. N. Naidu and L. Iyengar, Thermal Expansion of Rutile and Anatase, *J. Am. Ceram. Soc.*, 1970, **53**, 124–126.
48 M. E. Straumanis, T. Ejima and W. J. James, The TiO2 phase explored by the lattice constant and density method, *Acta Crystallogr.*, 1961, **14**, 493–497.
49 D. T. Cromer and K. Herrington, The Structures of Anatase and Rutile, *J. Am. Chem. Soc.*, 1955, **77**, 4708–4709.
50 J. K. Burdett, T. Hughbanks, G. J. Miller, J. W. Richardson and J. V. Smith, Structural-electronic relationships in inorganic solids: powder neutron diffraction studies of the rutile and anatase polymorphs of titanium dioxide at 15 and 295 K, *J. Am. Chem. Soc.*, 1987, **109**, 3639–3646.
51 H. J. Monkhorst and J. D. Pack, Special points for Brillouin-zone integrations, *Phys. Rev. B*, 1976, **13**, 5188.
52 T. S. Bjørheim, A. Kuwabara and T. Norby, Defect Chemistry of Rutile TiO2 from First Principles Calculations, *J. Phys. Chem. C*, 2013, **117**, 5919–5930.
53 X. Cai, P. Zhang and S.-H. Wei, Revisit of the band gaps of rutile SnO2 and TiO2: a first-principles study, *J. Semicond.*, 2019, **40**, 092101.
54 S.-D. Mo and W. Y. Ching, Electronic and optical properties of three phases of titanium dioxide: Rutile, anatase, and brookite, *Phys. Rev. B:Condens. Matter Mater. Phys.*, 1995, **51**, 13023–13032.
55 J. Pascual, J. Camassel and H. Mathieu, Resolved Quadrupolar Transition in TiO2, *Phys. Rev. Lett.*, 1977, **39**, 1490–1493.
56 J. Heyd, G. E. Scuseria and M. Ernzerhof, Hybrid functionals based on a screened Coulomb potential, *J. Chem. Phys.*, 2003, **118**, 8207–8215.
57 C. Freysoldt, B. Grabowski, T. Hickel, J. Neugebauer, G. Kresse, A. Janotti and C. G. Van de Walle, First-principles calculations for point defects in solids, *Rev. Mod. Phys.*, 2014, **86**, 253–305.
58 S. Lany and A. Zunger, Accurate prediction of defect properties in density functional supercell calculations, *Modell. Simul. Mater. Sci. Eng.*, 2009, **17**, 084002.
59 J. M. Adamczyk, L. C. Gomes, J. Qu, G. A. Rome, S. M. Baumann, E. Ertekin and E. S. Toberer, Native Defect Engineering in CuInTe2, *Chem. Mater.*, 2021, **33**, 359–369.
60 O. W. Johnson, S.-H. Paek and J. W. DeFord, Diffusion of H and D in TiO2: Suppression of internal fields by isotope exchange, *J. Appl. Phys.*, 1975, **46**, 1026–1033.
61 R. Krishna, Uphill diffusion in multicomponent mixtures, *Chem. Soc. Rev.*, 2015, **44**, 2812–2836.
62 W. Kern, in *Handbook of Silicon Wafer Cleaning Technology*, ed. K. A. Reinhardt and W. Kern, William Andrew Publishing, 3rd edn, 2018, pp. 3–85.
63 O. Berger, Understanding the fundamentals of TiO2 surfacesPart II. Reactivity and surface chemistry of TiO2 single crystals, *Surf. Eng.*, 2022, **38**, 846–906.
64 M. Králik, Adsorption, chemisorption, and catalysis, *Chem. Pap.*, 2014, **68**, 1625–1638.
65 A. P. St-Pierre, V. Shikon and D. C. Schneider, Count data in biology—Data transformation or model reformation?, *Ecol. Evol.*, 2018, **8**, 3077–3085.
66 M. Bylesjö, O. Cloarec and M. Rantalainen, in *Comprehensive Chemometrics*, ed. S. Brown, R. Tauler and B. Walczak, Elsevier, Oxford, 2nd edn, 2009, pp. 101–114.
67 E. Vittinghoff, C. E. McCulloch, D. V. Glidden and S. C. Shiboski, in *Handbook of Statistics*, ed. C. R. Rao, J. P. Miller and D. C. Rao, Elsevier, 2007, vol. 27, pp. 148–186.
68 Q. Zhang, A. M. Schmidt and Y. P. Chaubey, Modeling left-censored skewed spatial processes: The case of arsenic drinking water contamination, *Spat. Stat.*, 2024, **59**, 100816.
69 J. Li and A. D. Heap, Spatial interpolation methods applied in the environmental sciences: A review, *Environ. Modell. Software*, 2014, **53**, 173–189.

70 D. Ruppert, *International Encyclopedia of the Social & Behavioral Sciences*, Elsevier, 2001, pp. 15007–15014.
71 V. Corradi and N. R. Swanson, The effect of data transformation on common cycle, cointegration, and unit root tests: Monte Carlo results and a simple test, *J. Econom.*, 2006, **132**, 195–229.
72 M. J. Blanca, R. Alarcón, J. Arnau, R. Bono and R. Bendayan, Datos no normales: ¿es el ANOVA una opción válida?, *Psicothema*, 2017, **29**, 552–557.
73 M. M. Ali and S. C. Sharma, Robustness to nonnormality of regression F-tests, *J. Econom.*, 1996, **71**, 175–205.
74 T. Holsclaw, K. A. Hallgren, M. Steyvers, P. Smyth and D. C. Atkins, Measurement error and outcome distributions: Methodological issues in regression analyses of behavioral coding data, *Psychol. Addict. Behav.*, 2015, **29**, 1031–1040.
75 M. P. Perme and D. Manevski, Confidence intervals for the Mann–Whitney test, *Stat. Methods Med. Res.*, 2018, **28**, 3755–3768.
76 H. Jeong, E. G. Seebauer and E. Ertekin, First-principles description of oxygen self-diffusion in rutile TiO2: Assessment of uncertainties due to enthalpy and entropy contributions, *Phys. Chem. Chem. Phys.*, 2018, **20**, 17448–17457.
77 H. Peng, First-principles study of native defects in rutile TiO2, *Phys. Lett. A*, 2008, **372**, 1527–1530.
78 H.-Y. Lee, S. J. Clark and J. Robertson, Calculation of point defects in rutile TiO_2 by the screened-exchange hybrid functional, *Phys. Rev. B:Condens. Matter Mater. Phys.*, 2012, **86**, 75209.
79 L.-B. Mo, Y. Wang, Y. Bai, Q.-Y. Xiang, Q. Li, W.-Q. Yao, J.-O. Wang, K. Ibrahim, H.-H. Wang, C.-H. Wan and J.-L. Cao, Hydrogen Impurity Defects in Rutile TiO2, *Sci. Rep.*, 2015, **5**, 17634.
80 T. S. Bjørheim, S. Stølen and T. Norby, Ab initio studies of hydrogen and acceptor defects in rutile TiO2, *Phys. Chem. Chem. Phys.*, 2010, **12**, 6817–6825.
81 P. W. Peacock and J. Robertson, Behavior of hydrogen in high dielectric constant oxide gate insulators, *Appl. Phys. Lett.*, 2003, **83**, 2025–2027.
82 E. V. Lavrov, T. Mchedlidze and F. Herklotz, Photoconductive detection of hydrogen in ZnO and rutile TiO2, *J. Appl. Phys.*, 2016, **120**, 055703.
83 J. Weber, E. V. Lavrov and F. Herklotz, Hydrogen shallow donors in ZnO and rutile TiO2, *Phys. B*, 2012, **407**, 1456–1461.
84 A. Janotti and C. G. Van de Walle, Native point defects in ZnO, *Phys. Rev. B:Condens. Matter Mater. Phys.*, 2007, **76**, 165202.
85 J. L. Lyons, J. B. Varley, D. Steiauf, A. Janotti and C. G. Van de Walle, First-principles characterization of native-defect-related optical transitions in ZnO, *J. Appl. Phys.*, 2017, **122**, 035704.
86 E. J. Skiba, H. B. Buckner, C. Lee, G. McKnight, R. F. Wallick, R. van der Veen, E. Ertekin and N. H. Perry, UV-Driven Oxygen Surface Exchange and Stoichiometry Changes in a Thin-Film, Nondilute Mixed Ionic Electronic Conductor, Sr(Ti,Fe)O3-d, *J. Am. Chem. Soc.*, 2024, **146**, 23265–23277.
87 K. Alberi and M. A. Scarpulla, Effects of excess carriers on charged defect concentrations in wide bandgap semiconductors, *J. Appl. Phys.*, 2018, **123**, 185702.
88 R. Vaidyanathan, S. Felch, H. Graoui, M. A. Foad, Y. Kondratenko and E. G. Seebauer, Nonthermal illumination effects on ultra-shallow junction formation, *Appl. Phys. Lett.*, 2011, **98**, 194104.
89 E. G. Seebauer, M. Y. L. Jung, C. T. M. Kwok, R. Vaidyanathan and Y. V. Kondratenko, Measurement of photostimulated self-diffusion in silicon, *J. Appl. Phys.*, 2011, **109**, 103708.
90 J. Meng, M. S. Sheikh, R. Jacobs, J. Liu, W. O. Nachlas, X. Li and D. Morgan, Computational discovery of fast interstitial oxygen conductors, *Nat. Mater.*, 2024, **23**, 1252–1258.
91 I. M. Nadeem, C. Penschke, J. Chen, X. Torrelles, A. Wilson, H. Hussain, G. Cabailh, O. Bikondoa, J. Imran, C. Nicklin, R. Lindsay, J. Zegenhagen, M. O. Blunt, A. Michaelides and G. Thornton, Ultracompact Electrical Double Layers at TiO2(110) Electrified Interfaces, *J. Am. Chem. Soc.*, 2024, **146**, 33443–33451.
92 A. Selloni, Aqueous Titania Interfaces, *Annu. Rev. Phys. Chem.*, 2024, **75**, 47–65.
93 B. B. Nielsen, K. Tanderup, M. Budde, K. B. Nielsen, J. L. Lindström, R. Jones, S. Öberg, B. Hourahine and P. R. Briddon, Local Vibrational Modes of Weakly Bound O–H Complexes in SI, *Mater. Sci. Forum*, 1997, **258–263**, 391–398.
94 W. Luo, P. B. Rasband, P. Clancy and B. W. Roberts, Tight-binding studies of the tendency for boron to cluster in c-Si. II. Interaction of dopants and defects in boron-doped Si, *J. Appl. Phys.*, 1998, **84**, 2476–2486.
95 J. Yu, X.-M. Bai, A. El-Azab and T. R. Allen, Oxygen transport in off-stoichiometric uranium dioxide mediated by defect clustering dynamics, *J. Chem. Phys.*, 2015, **142**, 94705.
96 J. M. Flitcroft, M. Molinari, N. A. Brincat, N. R. Williams, M. T. Storr, G. C. Allen and S. C. Parker, The critical role of hydrogen on the stability of oxy-hydroxyl defect clusters in uranium oxide, *J. Mater. Chem. A*, 2018, **6**, 11362–11369.
97 G. Singh, M. Kaur, V. Kumar Garg and A. C. Oliveira, Oxygen hyper stoichiometric trimetallic titanium doped magnesium ferrite: Structural and photocatalytic studies, *Ceram. Int.*, 2022, **48**, 24476–24484.
98 J. K. Grewal, M. Kaur, R. K. Sharma, A. C. Oliveira, V. K. Garg and V. K. Sharma, Structural and Photocatalytic Studies on Oxygen Hyperstoichiometric Titanium-Substituted Strontium Ferrite Nanoparticles, *Magnetochemistry*, 2022, **8**, 120.
99 J. K. Cooper, S. B. Scott, Y. Ling, J. Yang, S. Hao, Y. Li, F. M. Toma, M. Stutzmann, K. V. Lakshmi and I. D. Sharp, Role of hydrogen in defining the n-type character of BiVO4 photoanodes, *Chem. Mater.*, 2016, **28**, 5761–5771.
100 A. Lushchik, V. N. Kuzovkov, E. A. Kotomin, G. Prieditis, V. Seeman, E. Shablonin, E. Vasil'chenko and A. I. Popov, Evidence for the formation of two types of oxygen

interstitials in neutron-irradiated α-Al2O3 single crystals, *Sci. Rep.*, 2021, **11**, 20909.

101 M. D. McCluskey, M. C. Tarun and S. T. Teklemichael, Hydrogen in oxide semiconductors, *J. Mater. Res.*, 2012, **27**, 2190–2198.

102 H. Li and J. Robertson, Behaviour of hydrogen in wide band gap oxides, *J. Appl. Phys.*, 2014, **115**, 203708.

103 M. E. Ingebrigtsen, A. Y. Kuznetsov, B. G. Svensson, G. Alfieri, A. Mihaila, U. Badstübner, A. Perron, L. Vines and J. B. Varley, Impact of proton irradiation on conductivity and deep level defects in β-Ga2O3, *APL Mater.*, 2019, **7**, 22510.

104 E. V. Lavrov, I. Chaplygin, F. Herklotz and V. V. Melnikov, Hydrogen Donors in Anatase TiO2, *Phys. Status Solidi B*, 2021, **258**, 2100171.

105 E. V. Lavrov, I. Chaplygin, F. Herklotz, V. V. Melnikov and Y. Kutin, Hydrogen in single-crystalline anatase TiO2, *J. Appl. Phys.*, 2022, **131**, 030902.

